Original Article

Vascularization and innervation of slits within polydimethylsiloxane sheets in the subcutaneous space of athymic nude mice

Journal of Tissue Engineering
Volume 8: 1–8

DOI: 10.1177/2041731417691645
journals.sagepub.com/home/tej
SAGE

Rachel E Gurlin[1], Mark T Keating[1], Shiri Li[2], Jonathan RT Lakey[1,2], Sébastien de Feraudy[3], Bhupinder S Shergill[1] and Elliot L Botvinick[1,2]

Abstract

Success of cell therapy in avascular sites will depend on providing sufficient blood supply to transplanted tissues. A popular strategy of providing blood supply is to embed cells within a functionalized hydrogel implanted within the host to stimulate neovascularization. However, hydrogel systems are not always amenable for removal post-transplantation; thus, it may be advantageous to implant a device that contains cells while also providing access to the circulation so retrieval is possible. Here we investigate one instance of providing access to a vessel network, a thin sheet with through-cut slits, and determine if it can be vascularized from autologous materials. We compared the effect of slit width on vascularization of a thin sheet following subcutaneous implantation into an animal model. Polydimethylsiloxane sheets with varying slit widths (approximately 150, 300, 500, or 1500 µm) were fabricated from three-dimensional printed molds. Subcutaneous implantation of sheets in immunodeficient mice revealed that smaller slit widths have evidence of angiogenesis and new tissue growth, while larger slit widths contain native mature tissue squeezing into the space. Our results show that engineered slit sheets may provide a simple approach to cell transplantation by providing a prevascularized and innervated environment.

Keywords

Subcutaneous implant, vascularization, innervation, polydimethylsiloxane, micro-stereolithographic three-dimensional printing

Date received: 11 October 2016; accepted: 11 January 2017

Introduction

Vascularization of scaffolds and implanted materials has been a major topic of study in the field of tissue engineering for the past several decades.[1,2] Notably, cell therapies, in which autologous or foreign tissues are transplanted, are emerging as complementary or replacement options to a myriad of ailments and diseases. In cell therapy, whole organ transplantation is replaced by transplantation of the constitutive or engineered cells, often free from the stroma and frequently, without perfused vasculature. One promising approach is to embed these cells within a three-dimensional (3D) scaffold, which can provide mechanical support, and potentially access to the host vasculature for exchange of oxygen, carbon dioxide, metabolites, and

[1]Department of Biomedical Engineering, University of California, Irvine, Irvine, CA, USA
[2]Department of Surgery, School of Medicine, University of California, Irvine, Irvine, CA, USA
[3]Department of Dermatology, School of Medicine, University of California, Irvine, Irvine, CA, USA

Corresponding authors:
Elliot L Botvinick, Department of Biomedical Engineering, University of California, Irvine, 2416 Engineering Hall, Irvine, CA 92697-2730, USA.
Email: elliot.botvinick@uci.edu

Bhupinder S Shergill, Department of Biomedical Engineering, University of California, Irvine, 2150 Engineering Hall, Irvine, CA 92697-2730, USA.
Email: bshergil@uci.edu

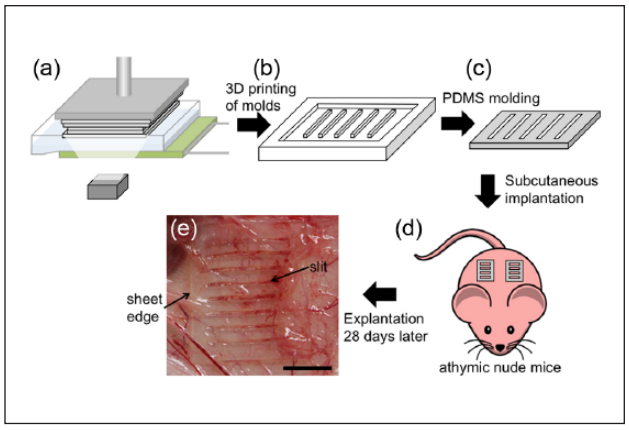

Figure 1. Sheet fabrication, implantation, and explantation process. (a) A micro-stereolithographic 3D printer creates molds layer by layer. (b) Molds are filled with PDMS to create the sheet implants (c) with various slit widths. (d) Two sheets are implanted into the subcutaneous space of each athymic nude mouse. (e) At 28 days, the skin flap shows vessel infiltration around the 500 µm slit size implant, scale bar: 5 mm.

waste. Thus, considerable advances have been made to promote invasion of the host vasculature into these scaffolds in an effort to improve cell viability and function. Many groups have investigated various approaches such as the use of proangiogenic factors, progenitor cells, vascular-inductive biomaterials, bioreactors, microelectromechanical system (MEMS)-related approaches, and combinations of these methods to promote neovascularization and angiogenesis.[3,4] Important to our study, others have shown that the geometry of an implant, and not chemical factors alone, also plays a role in forming vascular networks.[5–7]

Polydimethylsiloxane (PDMS) has long been used for medical device implants in addition to creating tissues,[8] promoting vessel growth,[9,10] and regenerating nerves[11] in vivo. PDMS is considered to be biocompatible and has other advantages such as low cost, optical transparency, flexibility, and durability. PDMS is a good candidate material for tissue engineering strategies that require biocompatibility and non-resorption over time. On the other hand, physical geometries and shapes, mainly microchannels, have also been used to encourage vascularization[5,7,12,13] and nerve growth[13–16] in vivo. We investigate if this biocompatible material cast into thin sheet containing rectangular slits can promote healthy tissue growth in vivo (Figure 1). A subcutaneous implantation site allows for easy retrieval and removal of cells; therefore, a thin profile is desirable, as to not introduce excessive strain on the tissue. The purpose of this study was to investigate the thin sheet slit architecture as a way to use the host's own tissue response in creating a perfused microvascular network in vivo. Tissue response was evaluated by implanting PDMS sheets with different slit widths in the subcutaneous space of immunodeficient mice. Subsequently, the sheets were removed, histologically processed, and analyzed.

Materials and methods

Sheet fabrication

Thin sheets of PDMS (Sylgard® 184 Silicone Elastomer Kit, Dow Corning Corp., Midland, MI, USA), each containing a parallel array of slits, were fabricated by polymerization within a custom mold. All slits within each sheet were of approximately equal width: 150, 300, 500, or 1500 µm. Molds were designed in SolidWorks (Dassault Systemes Solidworks Corp., Waltham, MA, USA), exported to an STL file, and printed by a high-resolution stereolithography 3D printer (Pico Plus 27, Asiga, Anaheim Hills, CA, USA). The mold was made of a hard 405-nm light curable resin (PlasCLEAR, Asiga), with x- and y-resolutions of 27 µm, and fabricated layer-by-layer in 10-µm-thick slices (Figure 1(a)). After the build was finished, molds were washed three times in isopropanol and sonicated for 10 min in isopropanol to remove any uncured resin. Molds were air dried for 15 min, then further cured by 10 min exposure to an 8W 302 nm UV light source (Dual UV Transilluminator, VWR International, Radnor, PA, USA), and subsequently baked in an oven overnight at 80°C. Finally, liquid PDMS (1:10 ratio of crosslinker to monomer base) was poured into the molds and baked at 80°C for 2 h (Figure 1(b)). The polymerized thin sheets (Figure 1(c)) were removed from the molds and autoclaved at 122°C for 20 min. All sheets had planar dimensions of approximately 14 mm × 22 mm and thickness 0.5 mm. Slits were placed such that the space between neighboring slit edges was 1 mm.

In vivo study

Approximately 8-week-old male athymic nude mice (Charles River Laboratories, Inc., Wilmington, MA, USA) weighing between 20 and 25 g were used in this study. All procedures were approved by the UC Irvine Institutional Animal Care and Use Committee (IACUC #2008-2850). Animals were anesthetized with 2%–4% isoflurane for surgical experiments. A midline incision through the dorsal skin was created via sterile surgical scissors and two subcutaneous pockets were created by blunt dissection, one on the left and one of the right side of the incision. A single sheet was placed within each pocket (Figure 1(d)), and then a drop of blood (5–10 µL) from a donor mouse was spread across the upper surface of the sheet (in situ) in order to fill the slits with clotted blood.[17,18] The pocket on the left side was sealed by sutures running between the bottom layer of subcutaneous tissue and the underlying muscle layer to prevent the sheets from shifting and overlapping each other. The dorsal incision was sutured closed and secured with surgical

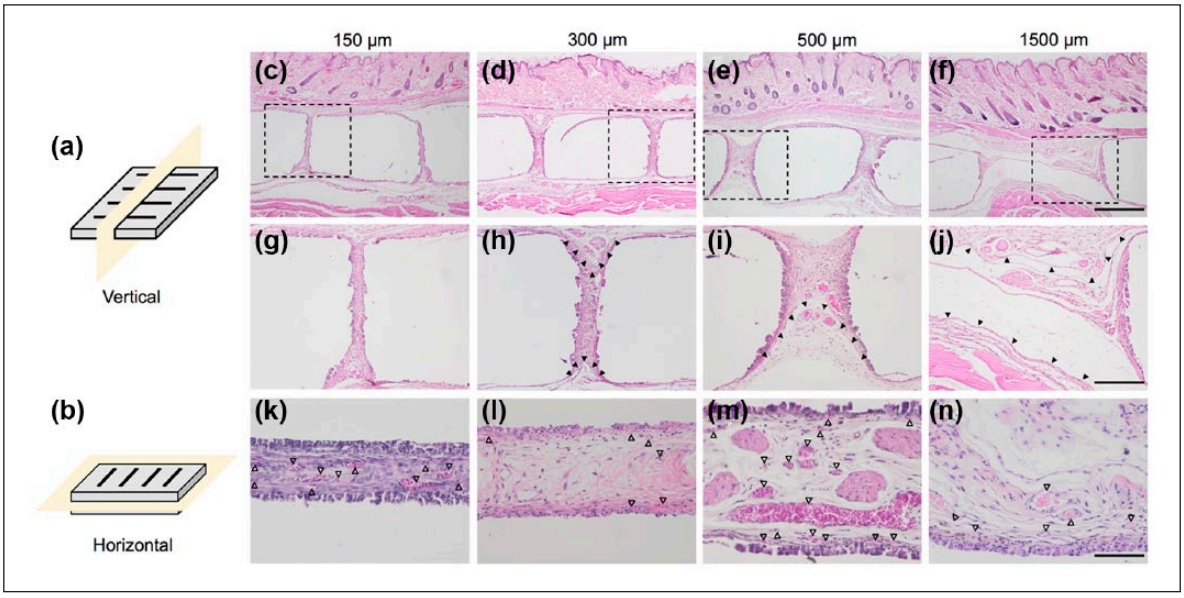

Figure 2. H&E staining reveals vascularized and innervated tissue. Samples were cut either in a vertical orientation (a) or in a horizontal orientation (b). Histological images post 28 days implantation into the subcutaneous space of athymic nude mice are shown for each slit width: (c, g, k) 150 µm, (d, h, l) 300 µm, (e, i, m) 500 µm, and (f, j, n) 1500 µm. Vertical sections at 4× magnification (c–f) are marked with a dashed rectangle, which were imaged again at 10× magnification (g–j). Arrows point to what appears to be invagination of native tissue into the slit space. Horizontal sections are shown in (k–n) at 20× magnification. Hollowed arrows point to erythrocyte-filled blood vessels. Scale bar: (c–f): 500 µm; (g–j): 200 µm; (k–n): 100 µm.

clips (Fine Science Tools, Inc., Foster City, CA, USA). The animals received ibuprofen, between 50 and 80 mg/kg, via drinking water for 2 days following surgery. Five animals were studied in each slit width group (150, 300, 500, and 1500 µm). Animals were monitored daily and after 28 days sheets were removed and animals were sacrificed (Figure 1(e)).

Histological preparation

Sheets were removed on day 28 by cutting through the full thickness of surrounding skin while leaving the tissue above and below the sheet intact. The excised tissue was immediately fixed by submersion in a 4% solution of phosphate-buffered formalin for 24 h. Samples were placed and sectioned in one of two orientations as illustrated in Figure 2(a) and (b). For each slit width, four sheets were placed for horizontal sectioning and one sheet for vertical sectioning. Vertical samples were prepared by first cutting the sheets with a trimming knife (Cancer Diagnostics, Inc., Durham, NC, USA) through their center in a direction transverse to the long axis of the slits and then transferring each half sheet into cassettes. Samples were processed and embedded within a paraffin block with the cut end facing the surface of the block (by Harris Histology Services, Tustin, CA, USA) and sectioned (Figure 2(a)). Horizontal samples were prepared by first cutting the sheets along the long axis of the center slit and then transferring each sheet half into cassettes. Samples were processed and blocked in paraffin wax with one half of the cut sheet with the skin facing the surface of the block and the other half with the muscle facing the surface of the block, side by side in one block (by Harris Histology Services) and sectioned (Figure 2(b)). Serial sections were cut (5 µm thickness) and mounted onto slides.

Histological and immunofluorescence staining

For histological observations, sections were stained with H&E. For immunohistochemistry, sections were deparaffinized followed by antigen retrieval via overnight incubation in 0.1 M Tris/HCl buffer, pH = 9.0 at 80°C.[19] Sections were then washed with phosphate-buffered saline (PBS), permeabilized with 0.5% Triton X-100, and blocked with 5% Donkey serum (Jackson ImmunoResearch, Inc., West Grove, PA, USA) for 30 min at room temperature. After serum blocking, slides were incubated with 1:200 monoclonal rabbit anti-alpha smooth muscle actin (αSMA) (Abcam, Cambridge, MA, USA) in 1× PBS supplemented with 5% Donkey serum and 0.5% Triton X-100 at 4°C overnight. Detection of peripheral nerve axons was performed with incubation of 1:400 polyclonal rabbit anti-S100 (Dako North America, Inc., Carpinteria, CA, USA). Slides were then washed with PBS and incubated with 1:500 AlexaFluor® 488 donkey anti-rabbit (Life Technologies, Carlsbad, CA, USA). Images were taken on an Olympus IX83 microscope at 20× with an Orca R2 camera (Hamamatsu Photonics K.K., Hamamatsu City, Japan) through MicroManager.[20]

Quantification of vessel and nerve count/ morphology

For analysis, H&E slides were imaged with a Nikon eclipse E800 microscope at 20× using Olympus cellSens Entry program. Images that contained vessels or nerve axons on multiple adjacent images were stitched together using Photoshop (Adobe Systems, Inc., San Jose, CA, USA). At least three slits were imaged for each slit size group. Images (or stitched images) for each slit were analyzed with a custom MATLAB (MathWorks, Inc., Natick, MA, USA) code for manual tracing of blood vessels and nerve tissue within each image and calculations of area and lengths of major and minor axes of the tracings. Vessels were identified by three criteria: (1) hollow lumen, (2) endothelial cell lining, and (3) luminal erythrocytes.[21–23] Nerve axonal tissue was identified by characteristic morphology: wavy bundles of eosinophilic fibers associated with spindled Schwann cells. Identifications and tracings were confirmed by a blinded dermatopathologist. The vessel (or nerve) area percentage or count was calculated as total vessel (or nerve) area or count divided by total slit tissue area. Circularity of vessels (or nerves) was defined as the length of the minor axis divided by the length of the major axis.

Statistical analysis

Prism 6 (GraphPad Software, Inc., La Jolla, CA, USA) was used for graphing and statistical testing. Data did not pass tests for normality necessitating non-parametric Kruskal–Wallis tests followed by post hoc Dunn's multiple comparisons test. Tests were determined statistically significant when $p < 0.05$. Vertical and horizontal section data were analyzed separately. Data represented by box plots show the median, IQR (interquartile range), and maximum and minimum values or 1.5IQR, whichever is shorter. Data represented by bar plots show the median ± IQR.

Results

Sheets were fabricated as described in section "Materials and methods" (Figure 1(a)–(c)) and implanted in pairs in the subcutaneous space along the back of male nude mice (Figure 1(d)). Animals tolerated the implants well, showing no changes in eating habits or signs of discomfort. No adverse reactions such as infection or necrosis were observed out to 28 days post-implantation. Digital photographs of sheets during explantation indicated local vascularization. Note that vessels can be resolved through the transparent sheet indicating the lack of thick fibrotic and opaque tissue at the sheet surface (Figure 1(e)). H&E staining of both vertical (Figure 2(a), (c)–(j)) and horizontal (Figure 2(b), (k)–(n)) sections showed host tissue infiltration within the slit space including erythrocyte-filled blood vessels and nerve tissue. On vertical sections through the larger slits (300, 500, and 1500 μm), the upper and lower region of each slit contains vessels, nerves, connective tissue, and muscle, suggesting that mouse superior and inferior dermis have squeezed into the larger slits (Figure 2(d)–(f), (h)–(j)). Tissue within all slits exhibits a foreign body response comprising macrophages and multinucleated giant cells in contact with the material edges. The presence of mature vessels (Figure 3(a)) and Schwann cells[24] (Figure 3(b)) was confirmed by immunohistochemistry staining for αSMA (Figure 3(c)) and S100 (Figure 3(d)), respectively.

Examination of all detected vessels in horizontal slices shows that tissue within the 1500 μm slits contains vessels with larger cross-sectional area as compared to the other groups (Figure 4(a)), and vessels within the 500 μm slits were of significantly smaller area as compared to the other groups. While differences in area were statistically significant, the physiological implications may be subtle, and absolute values of vessel area are consistent with other studies on vascularization of scaffolds.[22,25] No statistically significant differences in vessel area were found for vertical sections. Similarly, when investigating vessel circularity (Figure 4(b)) across all detected vessels in horizontal slices, we found that the 1500 μm slits contained vessels of greater circularity as compared to the other groups. In interpretation of circularity, it should be considered that circularity is dependent not only on vessel shape but also on the orientation of the vessel relative to the plane of sectioning. Assuming that vessels are on average circular in cross section, vessels that appear round (circularity $\cong 1$) likely run more perpendicular to the direction of sectioning as compared to those appearing oblong (circularity < 1), which may have a long axis at an angle to the section. Next, we compared vessel count and total vessel area percentage between multiple slits of the same width. For each individual slit, we determined total vessel count normalized by total slit area (Figure 4(c)), as well as the percentage of slit area occupied by vessels (Figure 4(d)). Interestingly, vessel count per slit area appears to decrease with increasing slit width (in both horizontal and vertical sections), and a statistically significant difference was detected between the 150 and 1500 μm groups. No trends or statistical differences were observed for percent vessel area.

Nerve axons were analyzed using the same metrics as for vessels. No nerves were detected within 150-μm-wide slits, but were detected within wider slits. While horizontal sections show nerves in the 300 μm slits had significantly larger areas as compared to those in the 500 μm slits (Figure 5(a)), this difference is biased by the unusually large nerve found in the 300 μm slit. In horizontal sections, nerve circularity within 300-μm-wide slits (Figure 5(b)) was significantly lower than that for the wider slits, a similar trend was observed for vertical sections. Next we

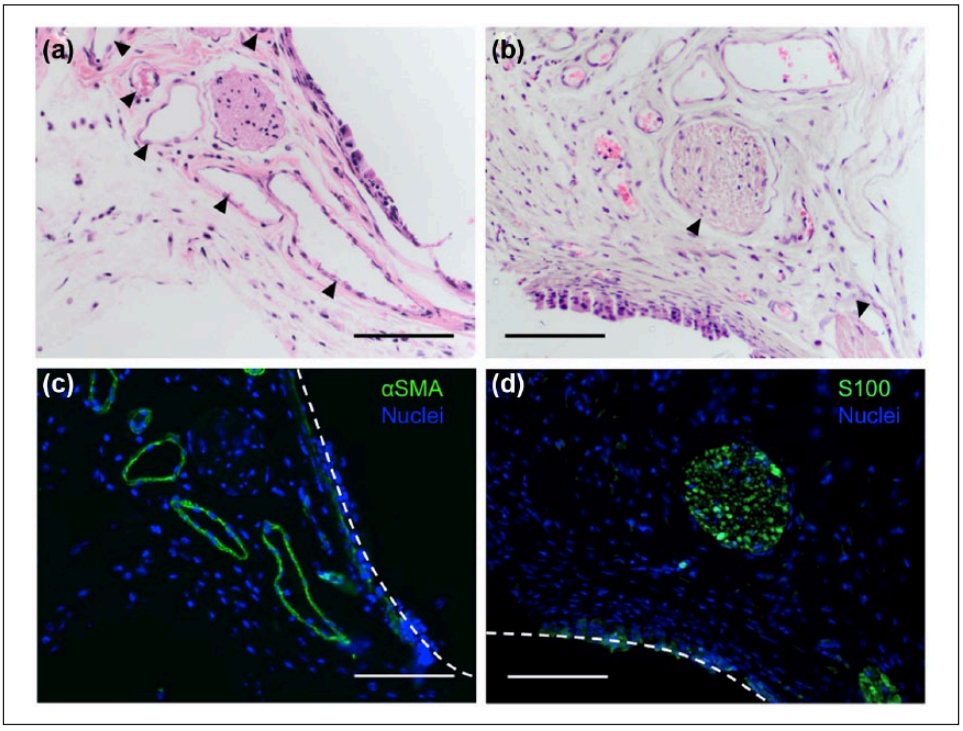

Figure 3. Immunohistochemistry detects both mature blood vessels and nerve tissue. Vertical sections of 500 µm slit samples were stained with H&E where arrows indicate (a) blood vessels or (b) nerves. The presence of (c) mature blood vessels via αSMA and (d) nerves via S100 were confirmed with immunohistochemistry of serial sections. Dashed white lines indicate the border of the material and tissue interface. Scale bar = 100 µm.

investigated variability in nerve count and total area between multiple slits of the same width. For each individual slit, we determined total nerve count normalized by total slit area (Figure 5(c)), as well as the percentage of total slit area occupied by nerves (Figure 5(d)). No trends were observed for nerve percent area.

Discussion

In this work, we describe a method to fabricate thin sheet silicone devices with varying slit widths to harness the host's tissue response to not only vascularize but also innervate an implant. Using a micro-stereolithographic printer for the quick prototyping of molds, sheets can be easily reconfigured (e.g. for slit width) and prototyped with PDMS or alternatively other moldable materials.

Tissue within slits contained nerve axons after 28 days of subcutaneous implantation. While the presence of nerve tissue in a device or scaffold typically indicates healthy tissue, it remains unclear if these nerve axons were formed de novo after implantation, or if they belong to native tissue that has fallen into the slits. There is conflicting evidence as to which mechanism is likely at day 28. A study of an engineered skin[26] implanted at the site of a full-thickness skin excision in nude mice shows absence of nerve tissue on day 40, with sparse innervation observed by day 60. This result suggests that insufficient time has passed for the de novo formation of nerve tissue in the slits and that only native nerve tissue is present. Conversely, new nerve tissue has been detected at day 28 in porcine-derived extracellular matrix scaffolds implanted intramuscularly within the rat abdominal wall[27] as well as in regenerated silk fibroin scaffolds implanted subcutaneously in immune-competent mice.[28] Relevant to these findings, slits in our sheets also contain a scaffold comprising fibrin polymerized from fibrinogen and other factors of autologous blood loaded into our sheets during implantation. Thus, there is a possibility that we observe new nerves at day 28.

To help elucidate which mechanism is responsible for innervation, we examined H&E-stained histological slides and notice, unexpectedly, what appears to be native tissue within slits that is innervated. This putative native tissue seems confined to the distal and proximal slit opening (Figure 2(h), black arrows) for the 300-µm-wide slits and penetrates increasing deeper within 500- and 1500-µm-wide slits (Figure 2(i) and (j), black arrows). The relationship between slit width and native tissue penetration is consistent with the fact that resistance of tissue to physical deformation into the narrow slits will increase with decreasing slit width. If this were the case, and if nerves were exclusively from native tissue, then we would expect at some

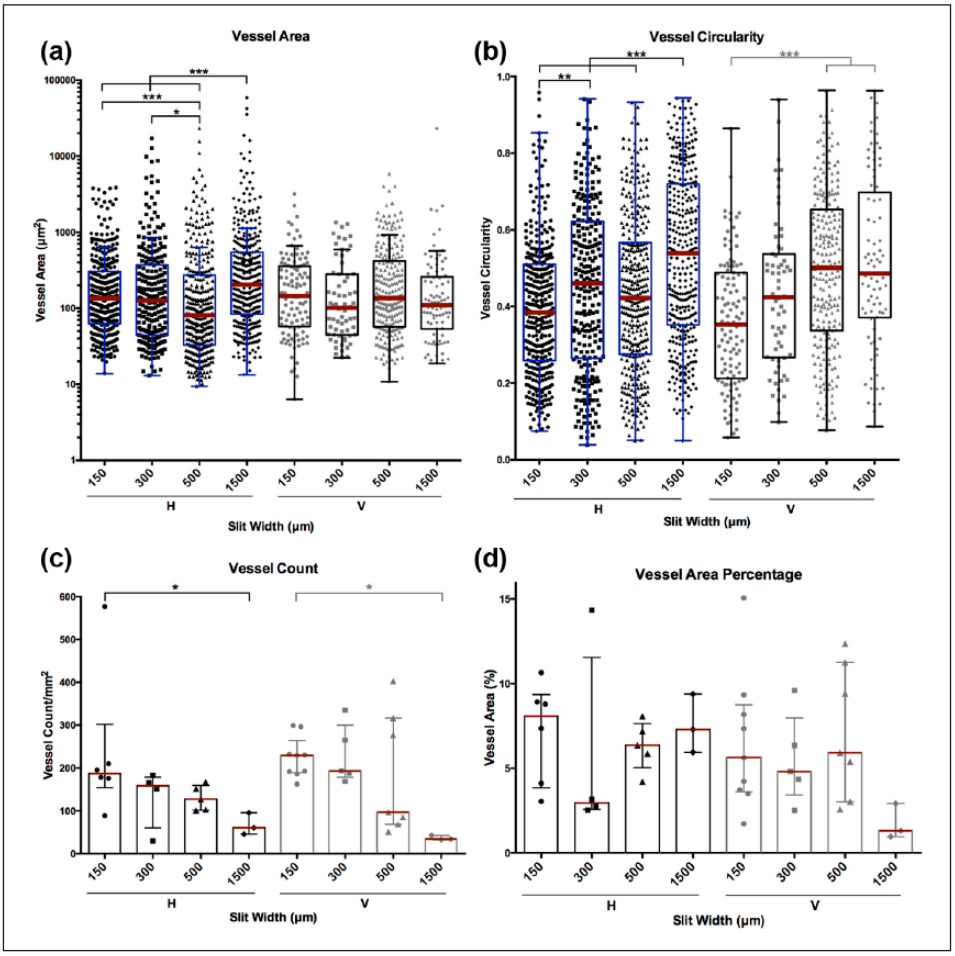

Figure 4. Quantification and comparison of vessel area, circularity, count, and area percentage within each slit width (150, 300, 500, 1500 μm) for both horizontal (H) and vertical (V) sections. Aggregate data of every detected vessel across all examined slit widths for (a) vessel area and (b) circularity. Each data point corresponds to a single vessel. The box plots show median (red), IQR (box), and 1.5IQR (or max and min values; whichever is shorter (whiskers)). Per slit, (c) the number of vessels per square millimeter tissue area and (d) the percentage of vessel area normalized by the total tissue area were quantified. Each data point is for a single slit. Data represent the median ± IQR. Statistical differences are indicated by ***$p < 0.001$, **$p < 0.01$, and *$p < 0.05$.

critical slit width that no nerves would be detected. In support of this notion, the 150-μm-wide slits alone did not indicate infiltration of native tissue and excluded nerves.

These same 150-μm-wide slits do contain a dense population of blood vessels, which normally form by angiogenesis during wound healing. Considering that blood within the slits forms a fibrin scaffold known to support angiogenesis, we speculate angiogenesis dominated vascularization in 150-μm-wide slits, whereas both native and new vessels penetrated the 300- and 500-μm-wide slits. In support of this, we found more vessels per cross-sectional area in the narrower slits (Figure 4(c)), indicating that de novo vascularized tissue was formed containing vessels typically smaller than those observed in 1500-μm-wide slits that contain native tissue (Figures 4(a) and 2(g)–(j)). Interestingly, no matter the slit size, the tissue still maintains similar vessel area percentage (Figure 4(d)), which may be a critical finding with respect to the design of cell therapy devices because narrower slits increase the remaining area of the sheet available to house transplanted cells.

Finally, and importantly, our method exploits the host's own tissue response to vascularize and innervate an implant without the need for synthetic hydrogels or exogenous proangiogenic factors. Additionally, we observed vessel area percentage values ranging from 1.3% to 8.1%, which are similar to that reported for other scaffolds.[21,29,30] Thus, our approach of utilizing the body's own response to promote tissue infiltration into a thin sheet not only provides a dense vasculature, but will not be considered a drug-device combination product by regulatory agencies. To the best of our knowledge, this is the first study to investigate rectangular slit architecture in promoting tissue growth. Numerous geometries have been investigated previously, the most common being pores or microchannels with spherical or cylindrical shapes.[5,6,10,12–16,22]

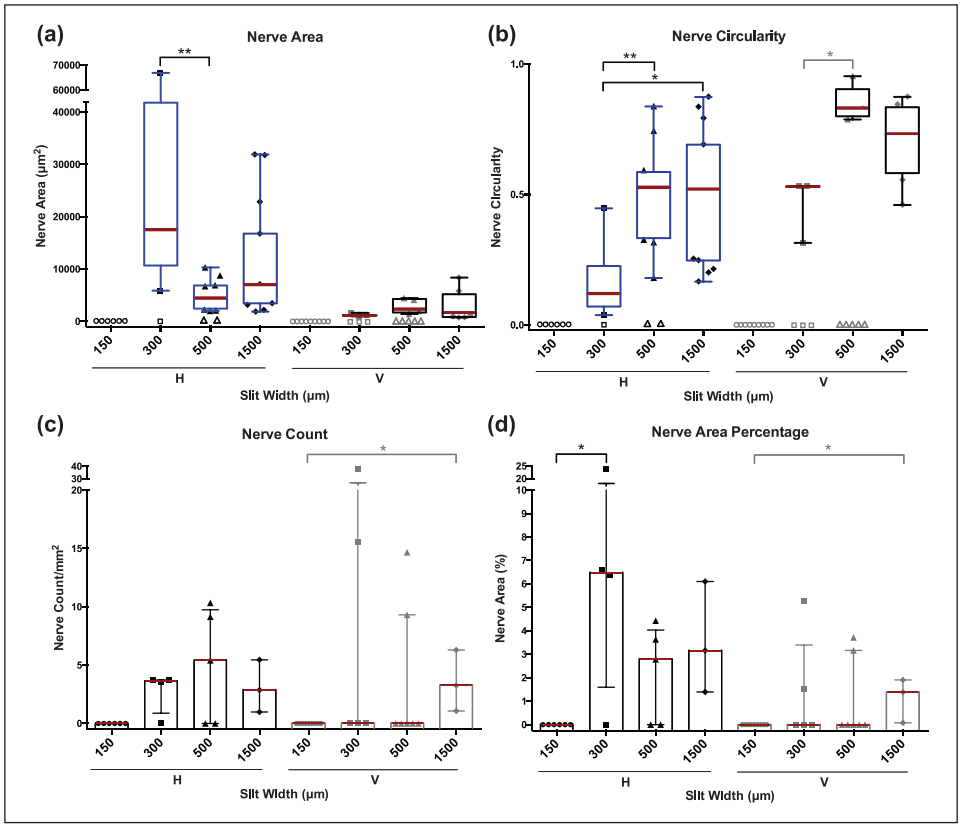

Figure 5. Quantification and comparison of nerve area, circularity, count, and area percentage in each slit width (150, 300, 500, 1500 μm) for both horizontal (H) and vertical (V) sections. Aggregate data of every detected nerve across all examined slit widths for (a) vessel area and (b) circularity. Each data point corresponds to a single nerve. Hollow symbols indicate that no nerves were detected in an individual slit. The box plots show the median, IQR (box), and 1.5IQR (or max and min values; whichever is shorter). Per slit, (c) the number of nerves per square millimeter tissue area and (d) the percentage of nerve area over the total tissue area were quantified. Each data point is for a single slit. Data represent the median ± IQR. Statistical differences are indicated by ***$p < 0.001$, **$p < 0.01$, and *$p < 0.05$.

Our findings demonstrate that rectangular slits are also a suitable geometry for promoting subcutaneous tissue infiltration. In general, the 150-μm-wide slits may be preferred over the wider slits if a vascularized, but not necessarily innervated, environment is required. On the other hand, the larger slit widths are more suitable to generate an innervated environment while remaining well vascularized. These results may be important for cell therapy devices in which vascularization is essential and nerve activity may be required.

Conclusion

Thin PDMS sheets with varying slit widths were molded via the simple and inexpensive technique of projection micro-stereolithography and implanted into the subcutaneous tissue of athymic nude mice. While no differences were found in blood vessel area percentage between the slit widths, vessel count did increase inversely with slit width likely due to active angiogenesis. We observed the infiltration of de novo tissue, an invagination of mature host tissue, or a combination of both. The presence of developed blood vessels and Schwann cells was confirmed by the expression of αSMA and S100, respectively. Further studies must be conducted to determine if results generalize to other tissue compartments such as the intramuscular space, omentum, or kidney capsule, or if our findings are exclusive to the subcutaneous space. In future work, sheets could contain openings or channels for cells to reside within the thickness of the sheet as a method for transplantation into a prevascularized and innervated network.

Acknowledgements

The authors would like to thank Rebecca Rowland, Paul de Vos, Bart de Haan, and Thuy Luu for their assistance in histology procedures. The authors would also like to acknowledge Michael Alexander for arranging animal surgeries.

Declaration of conflicting interests

The author(s) declared no potential conflicts of interest with respect to the research, authorship, and/or publication of this article.

Funding

The authors would like to acknowledge funding from the Iacocca Family Foundation (IFF-53627), NIH Laser Microbeam and Medical Program (LAMMP) (P41EB015890), Juvenile Diabetes Research Foundation (JDRF 17-2013-288), University of California, Irvine (UCI) Department of Surgery, and NIH T32 Cardiovascular Applied Research and Entrepreneurship (CARE) program (HL-116270) at the Edwards Lifesciences Center for Advanced Cardiovascular Technology at UCI for completion of this work.

References

1. Langer R and Vacanti JP. Tissue engineering. *Science* 1993; 260(5110): 920–926.
2. Auger FA, Gibot L and Lacroix D. The pivotal role of vascularization in tissue engineering. *Annu Rev Biomed Eng* 2013; 15: 177–200.
3. Phelps EA and García AJ. Engineering more than a cell: vascularization strategies in tissue engineering. *Curr Opin Biotechnol* 2010; 21(5): 704–709.
4. Lovett M, Lee K, Edwards A, et al. Vascularization strategies for tissue engineering. *Tissue Eng Part B Rev* 2009; 15(3): 353–370.
5. Stosich MS, Bastian B, Marion NW, et al. Vascularized adipose tissue grafts from human mesenchymal stem cells with bioactive cues and microchannel conduits. *Tissue Eng* 2007; 13(12): 2881–2890.
6. Chiu Y-C, Cheng M-H, Engel H, et al. The role of pore size on vascularization and tissue remodeling in PEG hydrogels. *Biomaterials* 2011; 32(26): 6045–6051.
7. Zhang W, Wray LS, Rnjak-Kovacina J, et al. Vascularization of hollow channel-modified porous silk scaffolds with endothelial cells for tissue regeneration. *Biomaterials* 2015; 56: 68–77.
8. Torisawa Y, Spina CS, Mammoto T, et al. Bone marrow-on-a-chip replicates hematopoietic niche physiology in vitro. *Nat Methods* 2014; 11(6): 663–669.
9. Pedraza E, Brady A-C, Fraker CA, et al. Macroporous three-dimensional PDMS scaffolds for extrahepatic islet transplantation. *Cell Transplant* 2013; 22(7): 1123–1135.
10. Clark RM, Cicotte KN, McGuire PG, et al. The effect of projection microstereolithographic fabricated implant geometry on myocutaneous revascularization. *Surg Sci* 2014; 5(12): 513–525.
11. Lundborg G, Gelberman RH, Longo FM, et al. In vivo regeneration of cut nerves encased in silicone tubes: growth across a six-millimeter gap. *J Neuropathol Exp Neurol* 1982; 41(4): 412–422.
12. Rnjak-Kovacina J, Wray LS, Golinski JM, et al. Arrayed hollow channels in silk-based scaffolds provide functional outcomes for engineering critically sized tissue constructs. *Adv Funct Mater* 2014; 24(15): 2188–2196.
13. Lee MK, Rich MH, Lee J, et al. A bio-inspired, microchanneled hydrogel with controlled spacing of cell adhesion ligands regulates 3D spatial organization of cells and tissue. *Biomaterials* 2015; 58: 26–34.
14. Stokols S, Sakamoto J, Breckon C, et al. Templated agarose scaffolds support linear axonal regeneration. *Tissue Eng* 2006; 12(10): 2777–2787.
15. Hossain R, Kim B, Pankratz R, et al. Handcrafted multilayer PDMS microchannel scaffolds for peripheral nerve regeneration. *Biomed Microdevices* 2015; 17(6): 109.
16. Moore MJ, Friedman JA, Lewellyn EB, et al. Multiple-channel scaffolds to promote spinal cord axon regeneration. *Biomaterials* 2006; 27(3): 419–429.
17. Soparkar CNS, Wong JF, Patrinely JR, et al. Growth factors embedded in an agarose matrix enhance the rate of porous polyethylene implant biointegration. *Ophthal Plast Reconstr Surg* 2000; 16(5): 341–346.
18. Sabini P, Sclafani AP, Romo T III, et al. Modulation of tissue ingrowth into porous high-density polyethylene implants with basic fibroblast growth factor and autologous blood clot. *Arch Facial Plast Surg* 2009; 2(1): 27–33.
19. Koopal SA, Coma MI, Tiebosch ATMG, et al. Low-temperature heating overnight in tris-HCl buffer pH 9 is a good alternative for antigen retrieval in formalin-fixed paraffin-embedded tissue. *Appl Immunohistochem* 1998; 6(4): 228–233.
20. Edelstein AD, Tsuchida MA, Amodaj N, et al. Advanced methods of microscope control using μManager software. *J Biol Methods* 2014; 1(2): e10.
21. Bloch K, Vanichkin A, Damshkaln LG, et al. Vascularization of wide pore agarose-gelatin cryogel scaffolds implanted subcutaneously in diabetic and non-diabetic mice. *Acta Biomater* 2010; 6(3): 1200–1205.
22. Choi SW, Zhang Y, Macewan MR, et al. Neovascularization in biodegradable inverse opal scaffolds with uniform and precisely controlled pore sizes. *Adv Healthc Mater* 2013; 2(1): 145–154.
23. Montazeri L, Hojjati-Emami S, Bonakdar S, et al. Improvement of islet engrafts by enhanced angiogenesis and microparticle-mediated oxygenation. *Biomaterials* 2016; 89: 157–165.
24. Mata M, Alessi D and Fink DJ. S100 is preferentially distributed in myelin-forming Schwann cells. *J Neurocytol* 1990; 19(3): 432–442.
25. Brudno Y, Ennett-Shepard AB, Chen RR, et al. Enhancing microvascular formation and vessel maturation through temporal control over multiple pro-angiogenic and pro-maturation factors. *Biomaterials* 2013; 34(36): 9201–9209.
26. Gingras M, Paradis I and Berthod F. Nerve regeneration in a collagen-chitosan tissue-engineered skin transplanted on nude mice. *Biomaterials* 2003; 24(9): 1653–1661.
27. Agrawal V, Brown BN, Beattie AJ, et al. Evidence of innervation following extracellular matrix scaffold mediated remodeling of muscular tissues. *J Tissue Eng Regen Med* 2009; 3(8): 590–600.
28. Liu Q, Huang J, Shao H, et al. Dual-factor loaded functional silk fibroin scaffolds for peripheral nerve regeneration with the aid of neovascularization. *RSC Adv* 2016; 6(9): 7683–7691.
29. Jiang B, Waller TM, Larson JC, et al. Fibrin-loaded porous poly(ethylene glycol) hydrogels as scaffold materials for vascularized tissue formation. *Tissue Eng Part A* 2012; 19(1–2): 224–234.
30. Freeman I and Cohen S. The influence of the sequential delivery of angiogenic factors from affinity-binding alginate scaffolds on vascularization. *Biomaterials* 2009; 30(11): 2122–2131.